
Supplementary information

Single-cell proteo-genomic reference maps of the hematopoietic system enable the purification and massive profiling of precisely defined cell states

In the format provided by the authors and unedited

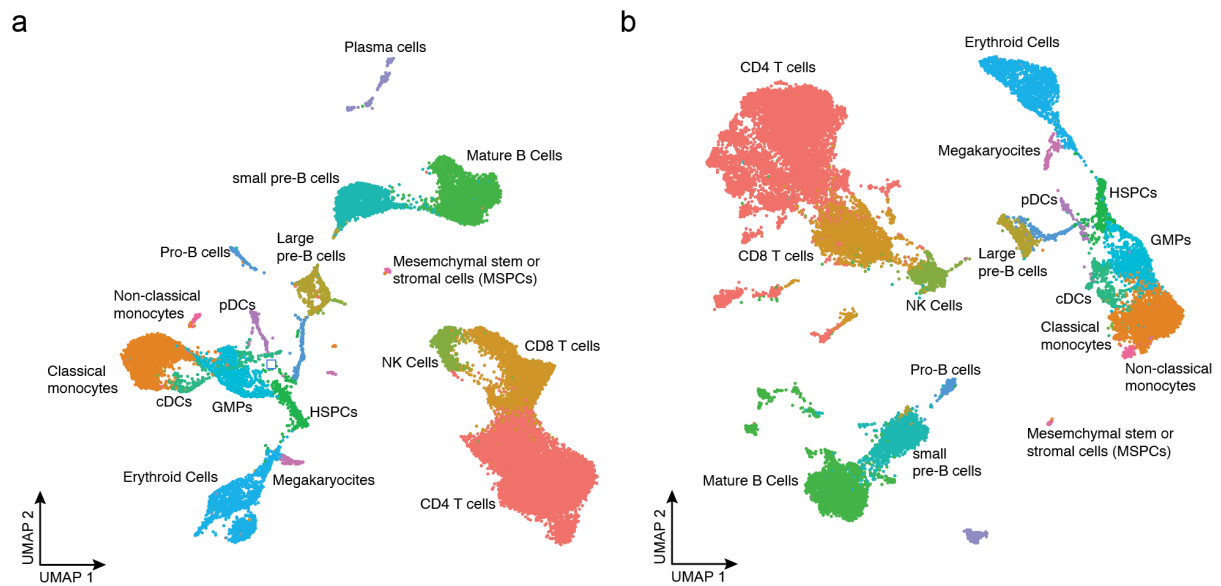
1	Supplementary Notes	
2		
3	Supplementary Note 1. Panel design for targeted transcriptomics	1
4	Supplementary Note 2: Whole transcriptome sequencing validates performance of the targeted	
5	panel.....	2
6	Supplementary Note 3: Effects of ultra-high plex antibody stainings and freeze-thaw cycles on	
7	gene expression	4
8	Supplementary Note 4: Analysis of sequencing requirements	6
9	Supplementary Note 5: Cell type annotation.....	7
10	Supplementary Note 6: Inclusion of surface marker data improves cell type classification.....	15
11	Supplementary Note 7: Validation of query datasets projections	16
12	Supplementary Note 8: Smart-seq2 validation	17
13	References	19

14

15 **Supplementary Note 1. Panel design for targeted transcriptomics**

16 In order to establish a comprehensive targeted transcriptomics approach in the human bone marrow, we
17 designed a panel that covers all cell types and differentiation stages of this organ. For this purpose, we
18 used one of the individuals from the human bone marrow dataset released by the Human Cell Atlas
19 project (Data obtained from Data Portal preview site:
20 <https://data.humancellatlas.org/explore/projects/cc95ff89-2e68-4a08-a234-480eca21ce79>). We filtered
21 out any cell for which fewer than 500 genes and more than 10% mitochondrial counts were detected.
22 We performed unsupervised clustering and UMAP-based dimensionality reduction on the 33.000 cells
23 that passed the quality filter. Subsequently, we annotated the cell types based on canonical markers from
24 the human bone marrow. We obtained 17 cell types covering all the main lineages in the hematopoietic
25 system (Figure N1a).

26



27
28

29 **Figure N1. Panel design for targeted single-cell transcriptomics of the human bone marrow.** Bone
30 marrow scRNA-seq data from a healthy individual was obtained from the Human cell atlas, the data
31 was processed and annotated. **a.** UMAP visualization of the whole transcriptome data highlighting the
32 result of unsupervised clustering. **b.** UMAP based on the 462 gene panel selected for Abseq highlighting
33 the clusters obtained in *a*.

34

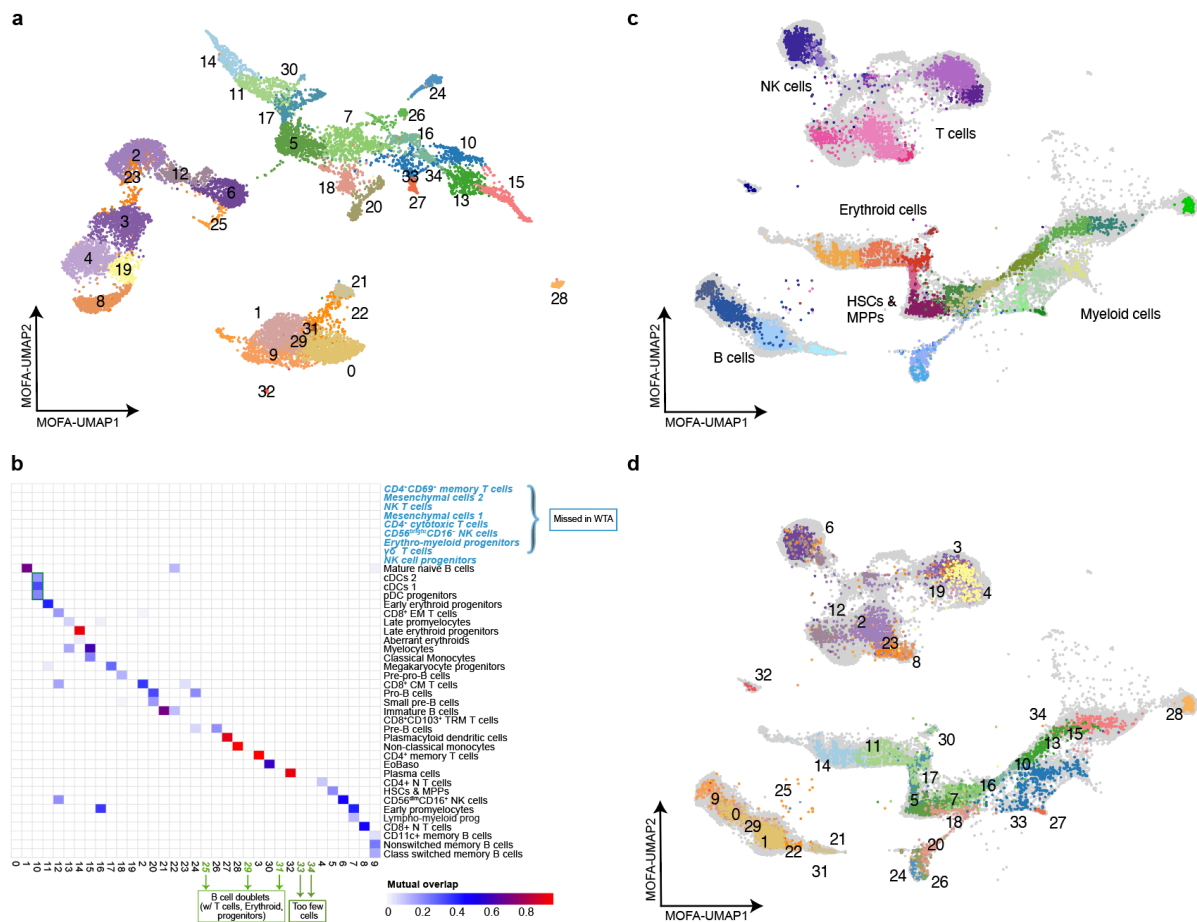
35 In order to identify a sparse, yet maximally informative set of marker genes, we followed the approach
36 for target selection in targeted single-cell transcriptomics developed previously (Schraivogel et al.,
37 2020). In short, we determined the genes that were differentially expressed between cell types and used
38 these as input to train a generalized linear model of cell type identity while applying a LASSO
39 regularization in order to select a maximally sparse set of features. Regularization parameters were
40 determined using 10-fold cross-validation. A total 257 genes were selected with this method. In addition
41 to these genes, we included 83 cell cycle markers (Kowalczyk et al., 2015), 88 genes corresponding to
42 the Abseq antibodies, and 75 genes with high variability in single-cell datasets of AML patients (Velten
43 et al., 2018). Due to a poor representation of hematopoietic stem and progenitor cells in the cell atlas
44 dataset, we complemented our targeted panel with 45 stem and progenitor cell markers previously
45 identified using a similar approach (Velten et al., 2017). All selected genes and primer sequences are
46 included in Supplementary Table 1. For primer design, a proprietary routine was followed (BD
47 Bioscience).

48 The selected panel allowed us to classify the cell types of the human cell atlas dataset with a 99,92% of
49 agreement and Cohen's kappa coefficient (κ) of 0.932. Moreover, we performed unsupervised clustering
50 and dimensionality reduction using only the selected genes for the panel (Figure N1b) and obtained a
51 partitioning highly similar to the clustering obtained when using whole-transcriptome data, as quantified
52 by an adjusted Rand index of 0.98. The performance of the panel was further validated by comparing
53 whole-transcriptome and targeted Abseq data (see Supplementary Note 2).

54 **Supplementary Note 2: Whole transcriptome sequencing validates performance of the targeted**
55 **panel**

56 In order to exclude that the targeted assay leads to biases in clustering or cell type annotation, we
57 performed whole transcriptome sequencing (WTA) together with profiling of the same 97 antibodies on
58 a sample from a healthy individual (Young3). For this, we processed 14,378 cells using the whole
59 transcriptome protocol for the BD Rhapsody system. On average we sequenced ~60,000 reads (i.e. 7x
60 deeper than with the targeted approach) for the RNA layer and 18,000 reads for the antibody layer per

61 cell. After normalizing the counts by the library size, the top 3,000 highly variable genes and all 97
 62 antibodies were used as input for the MOFA dimensionality reduction, unsupervised clustering, and
 63 UMAP calculations as described in the methods section. Thereby, 34 distinct clusters were identified
 64 (Figure N2a) Subsequently, we utilized the label transfer approach from Seurat v3 (Stuart et al., 2019)
 65 to predict the cell type identities using the targeted datasets as reference. We calculated the mutual
 66 overlap of the predicted labels with the unsupervised cluster (Figure N2b), and also projected the whole
 67 transcriptome data into the original reference space for comparison (Figure N2c, d and see also
 68 Supplementary Note 7). In the majority of cases, a 1:1 correspondence between clusters from the
 69 targeted approach and clusters from the whole transcriptome approach was observed. Some cell types
 70 were not covered in the WTA approach due to low cellular coverage. Together, these data suggest that
 71 our targeted panel resolves cell types equally well as the WTA approach at strongly reduced costs.
 72
 73

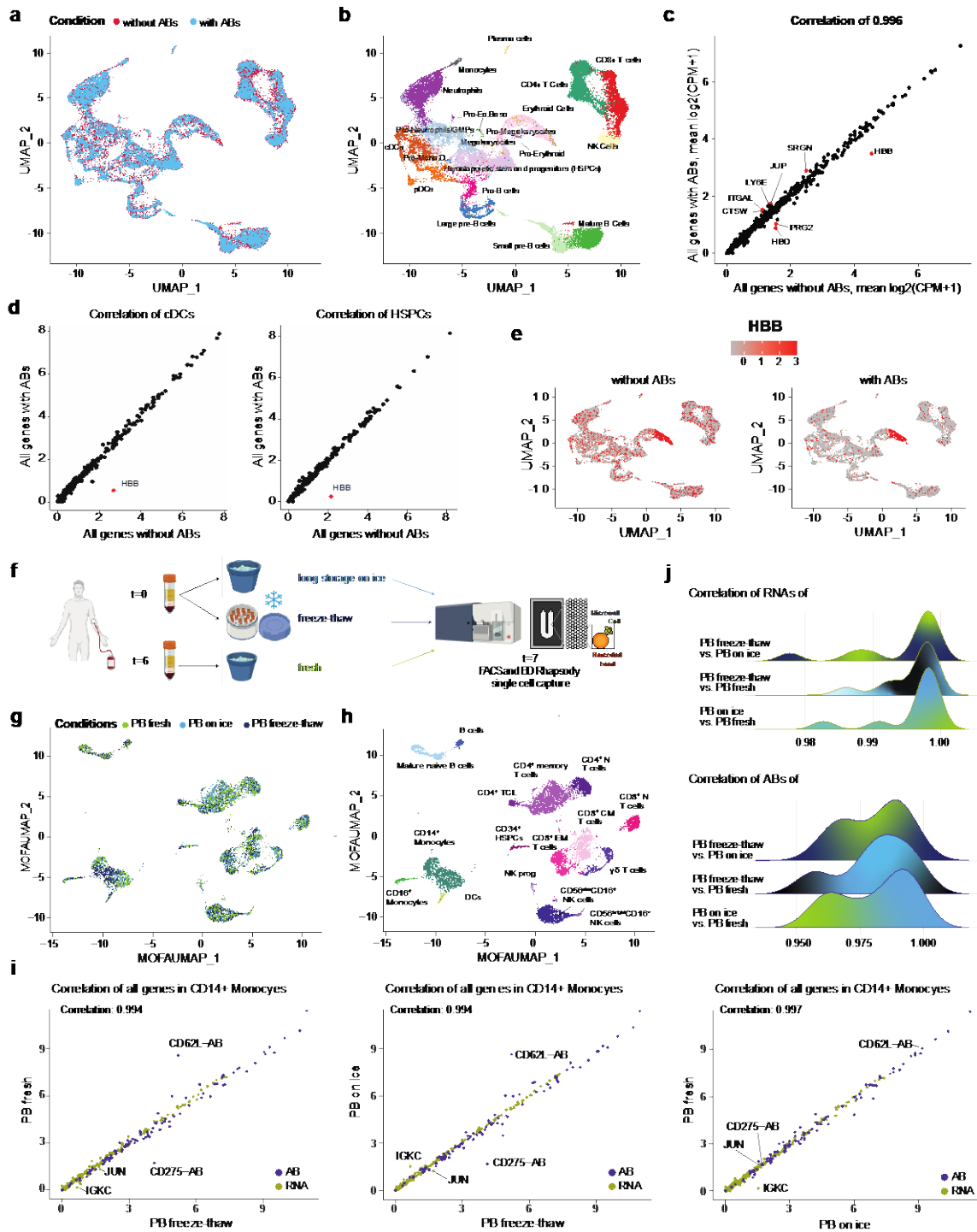


74
 75
 76 **Figure N2. Whole-transcriptome single-cell proteo-genomic sequencing.** **a.** MOFA-UMAP
 77 visualization of the whole transcriptome dataset colored by the unsupervised clusters. **b.** Mutuality
 78 analysis between the unsupervised clusters from the WTA and the identities predicted from the targeted
 79 datasets. Mutual overlap is defined as the product between the % of cells from a targeted cluster that
 80 form part of a given WTA cluster, and the % of cells from a WTA cluster that form part of a given
 81 targeted cluster. A mutual overlap of 1 indicates perfect overlap. **c.** Projection of the WTA samples in
 82 the healthy reference MOFA-UMAP space colored by predicted cell types **d.** and unsupervised clusters
 83 from **a.**
 84

85 **Supplementary Note 3: Effects of ultra-high plex antibody stainings and freeze-thaw cycles on**
86 **gene expression**

87 In order to exclude that staining live, primary cells with 97 antibodies affects gene expression, we
88 performed a control experiment. For this purpose, we used a sample from a healthy donor (Young1) and
89 proceeded as described in the Methods section ‘Cell sorting for Abseq’. Half of the sample was then
90 incubated with 97 Abseq antibodies, while the other half was left on ice. Finally, the BD Rhapsody
91 protocol was performed as described (see Methods ‘Abseq surface labeling, single-cell capture and
92 library preparation’). In order to compare both samples, only the transcriptomic information was
93 considered. We normalized the datasets, performed unsupervised clustering, and annotated the clusters
94 into major cell types from the bone marrow based on canonical markers (Figure N3a, b). All cell types
95 were present in both conditions without considerable batch effects driving any type of separation. The
96 correlation between the average expression of each gene between both samples was 0.996 (Figure N3c).
97 To account for possible slight variations in cell type abundance, we further investigated the correlation
98 between experiments at the level of individual cell types, and consistently found very high correlations
99 (see Figure N3d for representative examples). Only the erythroid-specific gene HBB, and to a lesser
100 extent HBD, were more abundantly observed in most cell types of the non-stained experiment,
101 suggesting that there is an elevated HBB background signal in this experiment. HBB is frequently
102 observed as ‘background’ in different single-cell RNA-seq studies (Young & Behjati, 2020). HBB
103 represents 96% of the RNA present in red blood cells and 80% of RNA in blood extracellular vesicles
104 (Kerkelä et al., 2019). Hence, cellular debris present in prepared samples mostly contains HBB,
105 explaining the abundance of this specific gene in the background signal. Here, the additional washes
106 included during the antibody staining apparently have helped to reduce the background signal.

107
108 The datasets established in this study was obtained from cryopreserved bone marrow cells. To evaluate
109 the effect of freeze-thaw cycles on gene- and surface antigen expression, we performed three control
110 experiments with peripheral blood mononuclear cells (PBMCs). Blood was drawn, subjected to Ficoll
111 density gradient centrifugation and PBMCs were frozen or left on ice for 6 hours; after this time interval,
112 blood was drawn again from the same donor and subjected to Ficoll density gradient centrifugation. All
113 three samples (PB fresh, PB on ice, PB freeze-thaw) were then processed together and living cells were
114 FACS-sorted and stained with 97 surface antibodies before single cell capture. Globally, correlations in
115 gene and surface antigen expression were very high (freeze-thaw vs. fresh = 0.994, freeze-thaw vs. on
116 ice = 0.994 and fresh vs. on ice = 0.997, Figure N3j). UMAP visualization of the data revealed that cell
117 types were unaffected by freezing except for the monocytes, showing a minor shift upon freeze-thawing
118 (Figure N3g, h). As a result of the freeze-thaw process, monocytes upregulated the T cell costimulatory
119 molecules CD275 (ICOS ligand) and the immediate early gene JUN, while downregulated the homing
120 receptor CD62L (SELL), indicative of a stress response (Figure N3i). Global gene expression patterns
121 remained unaffected. All in all, the freeze-thaw process had only a minor impact on our data. Specific
122 changes associated with freeze-thawing (such as for monocytes) apply equally for samples that have
123 been processed using the same pipeline.



125
 126 **Figure N3. Effects of ultra-high plex antibody stainings and freeze-thaw cycles on gene expression.**
 127 **a-e.** Comparison of a healthy bone marrow sample incubated with and without Abseq antibodies. **a, b.**
 128 A UMAP was generated on the targeted RNA single-cell profiles. The cells from either condition (*a*)
 129 and the annotated cell types (*b*) are highlighted. **c.** Correlation between the average expression of every
 130 gene in each sample; top differentially expressed genes are highlighted in red. **d.** Correlation between
 131 the average expression of every gene in two representative cell types (cDCs and HSPCs); HBB as most
 132 differentially expressed gene is highlighted in red **e.** UMAP visualization colored by the HBB expression
 133 in positive and negative samples. **f-j.** Comparison of fresh, frozen/thawed and iced PBMC samples. **f.**

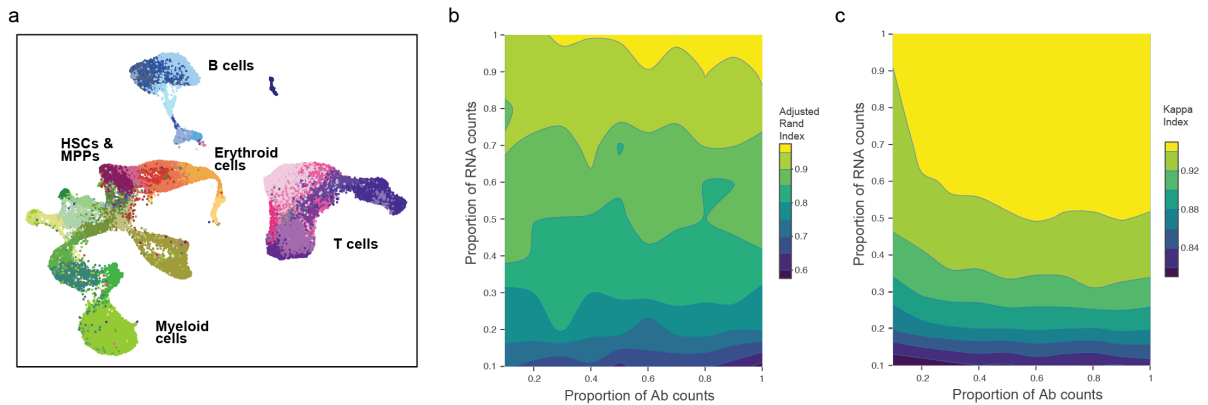
134 Overview of the experimental setup **g, h**. UMAPs were generated on the fresh, iced and freeze-thawed
135 PBMC samples sequenced with the 462 RNAs and 97 ABs targets. The cells are colored by their
136 condition (*g*) and cell type (*h*), respectively. **i**. Correlation between the average expression of each gene
137 per condition. Average expression of JUN, IGKC, CD276-AB and CD62L-AB are highlighted. **j**. Ridge
138 plots display the correlation coefficient of correlation between the average expression of every gene per
139 cell type and condition. Cell types which were represented by less than 50 cells were excluded from the
140 analysis.

141 **Supplementary Note 4: Analysis of sequencing requirements**

142 In order to establish the minimal sequencing requirements necessary to obtain an accurate cell type
143 classification, we down-sampled the RNA and AB counts of a healthy bone marrow sample (Young1)
144 and determined if this would yield a similar cluster structure using the same unsupervised clustering
145 pipeline as used for the non-down-sampled datasets. For illustration, data of all nine samples with an
146 average UMI count of 10,126 per cell (Figure 1b) were down-sampled to an average of 300 UMIs per
147 cell (60 UMIs antibodies, 240 UMIs RNA) (Figure N4a) and subsequently a UMAP was calculated.
148 This revealed that even much lower read numbers are sufficient to distinguish cell types and
149 differentiation states. While the total read/UMI counts may appear low compared to whole transcriptome
150 single-cell studies, it is in fact very deep for a targeted approach, as analyzed in detail in (Schraivogel
151 et al., 2020). To provide a more quantitative analysis, we performed down-sampling to different depths
152 and determined the overlap in cluster structure using the adjusted Rand index (Figure N4c).
153 Additionally, we used label transfers from the non-down-sampled dataset on the down-sampled dataset
154 to determine if cell types could be correctly classified. The agreement between the true labels and the
155 learnt labels was determined using Cohen's Kappa (Figure N4c). Both metrics showed that the RNA
156 counts were more important for the correct cell type identification and that we reached saturation with
157 around 70% of the RNA reads, i.e. an average read depth of 4,000 per cell. All samples were sequenced
158 to an average of ~8,500 reads for the mRNA libraries and ~12,000 reads per cell for the antibody
159 libraries. A more specific analysis on the benefit of profiling both surface markers and RNA for cell
160 type annotation, e.g. in the context of T cell populations, is presented in Supplementary Note 6.

161
162 We observed that some antibodies (e.g. CD18) occupy high percentages of reads whereas others are
163 lowly represented (e.g. CD20, see Extended Data Fig. 1). The large variation in reads per antibody is
164 not correlated with the fraction of cells positive for the antibody (e.g. both CD18 and CD20 are
165 expressed in 19% of cells, but CD18 has 63 times more reads), indicating that it is primarily related to
166 the abundance of the antigen on the surface, properties of the antibody, or properties of the panel. In
167 future, unlabeled antibodies of the same clone (also referred to as cold competitors) could be included
168 for highly represented antibodies to decrease the fraction of reads consumed by these antibodies and
169 thereby reduce the overall sequencing requirements. The data shown in Extended Data Fig. 1 (also
170 included in Supplementary Data 1) can be useful for selecting these antibodies in future studies.

171



173

174

175

176

177

178

Figure N4. Sequencing requirements. a. UMAP of the nine bone marrow samples down-sampled to an average of 300 UMIs (60 UMIs antibodies and 240 UMIs RNA). Cells are colored corresponding to *Figure 1b*. b, c. Effect of down-sampling RNA or antibody reads on cell type classification by (b) unsupervised clustering or (c) label transfer.

179

Supplementary Note 5: Cell type annotation

180

181

182

183

184

185

186

187

188

189

190

191

192

193

194

195

196

197

198

199

200

201

202

203

204

205

206

207

208

209

For cell type annotation, we used both information of the mRNA and cell surface antibody readouts. Especially for inter-connected clusters within the hematopoietic differentiation hierarchy and their branches along myeloid and lymphoid trajectories, fine gradients of surface marker expression and mRNA expression exist, which result in slight expression changes from one annotated cluster to the next. Supplementary Table 4 summarizes the surface markers and mRNAs used for annotation of the 45 clusters. For additional comparisons and analysis of differential mRNA and surface marker expression between any individual cluster of choice, usage of the Abseq-App and Supplementary Data 1 is highly recommended.

Hematopoietic stem cells and multipotent progenitors (HSCs & MPP) are defined via surface expression of CD34, CD133 and absence/lower levels of CD38, CD45RA and Tim3 expression. HSCs can be further characterized by robust CD90 and substantial CD4 expression. On the mRNA level, HSCs and MPPs were defined by high expression of CRHBP, NPR3, MEIS1, PROM1 and THY1 (Figure N5a). Erythro-myeloid progenitors (EMP) are emanating directly from the HSC and MPP cluster, maintain CD34 expression but lack CD133, CD38, CD4, CD11a or CD45RA surface expression. They are characterized via high expression of CPA3, FCER1A, DEPTOR and TESPA1 on the mRNA level (Figure N5a). Downstream of EMPs, early erythroid progenitors and late erythroid progenitors can be characterized by presence of CD34 and CD38 surface expression. Moreover, CD98 and CD326 start to be expressed at marked levels in early erythroid progenitors and further increase in late erythroid progenitors (Figure N5b). At the stage of the late erythroid progenitor cluster, surface expression of CD235 can be observed (Figure N5b). In addition, SOX4, APOC1, IL1B, CASP3 and SLC40A1 are highly expressed in early erythroid progenitors, whereas late erythroid progenitors highly express hemoglobins (HBB, HBD), CA1, BLVRB, AHSP and in later stages GYPA, encoding Glycophorin A. Of note, TFRC mRNA (encodes for transferrin receptor or CD71) starts to be highly expressed in EMPs and is constitutively expressed throughout erythroid differentiation. An additional erythroid cluster with enrichment in old and leukemic individuals could be observed next to late erythroid progenitors, termed aberrant erythroid cells, which was positive for CD235a, CD123, CD197 and CD90 surface and high levels of HBB, HBD, CA1, HEMGN, RHAG mRNA expression (Figure N5b). Megakaryocyte progenitors were defined by high surface expression of CD61 and CD49b and mRNA expression of PPBP, ITGA2B, PLEK, MPL, FERMT3 and SLC37A1 (Figure N5b). As shown previously, Eosinophil/Basophil progenitors showed similarities in gene expression with other cell types along the

210 erythroid differentiation trajectory, including high expression of CPA3 and FCER1A. Other genes
211 specifically expressed in this cell type are CLC, HDC, PRG2. Interestingly, RNASE2 and CPA3 are
212 also markedly expressed in Eosinophil/Basophil progenitors, but also expressed at high levels in cell
213 clusters along the myeloid differentiation trajectory (Figure N5b). Lympho-myeloid progenitors
214 emanate from the HSC & MPP cluster and were defined by their expression of CD34 and CD133,
215 absence/low levels of CD38 and dim expression of CD45RA, CD49b, Tim3, CD117 and in some cells
216 also CD10. On the transcriptomic level, cells within the Lympho-myeloid progenitor cluster expressed
217 high levels of FLT3, SPINK2, MZB1, ITM2C and MDK (Figure N5a).

218 Directly adjacent to the Lympho-myeloid progenitor cluster, early promyelocytes, that represent an
219 intermediate myeloid differentiation stage can be characterized by their surface expression of CD34,
220 CD38, CD133, CD117 and CD33 (Figure N5a and N5i). Signature genes highly expressed in the early
221 promyelocytes cluster comprise MPO, AZU1, CPA3, RNASE3, MGST and CEBPA. Following the
222 early promyelocytes stage, the subsequent myeloid differentiation stages are referred to as late
223 promyelocyte and myelocyte stages. In our dataset, cells within the late promyelocyte cluster gradually
224 lose CD34, CD133 and CD117 expression, whereas CD38 is increased and CD33 expression remains
225 at levels comparable to the early promyelocytes stage. Late promyelocytes can be further characterized
226 by their high transcriptomic expression of LYZ, CSTA and RNASE2, and slightly lower MPO and
227 AZU1 expression if compared to the early promyelocytes stage (Figure N5i). Myelocytes represent the
228 next transient myeloid differentiation stage, which lost their CD34 and CD133 surface expression, and
229 can be clearly distinguished from late promyelocytes by the emergence of CD11b expression on their
230 surface. Moreover, they highly express CD33 and CD11a and upregulate CD49e expression (Figure
231 N5i). They can be further characterized by high mRNA expression of S100A8, CSTA and S100A9.

232 Classical monocytes show overlap in their surface marker expression to myelocytes, however they
233 express additional markers like CD14, CD61 and CD32, and express higher levels of CD13 than their
234 progenitors (Figure N5i). On the transcriptomic level, classical monocytes highly express CD14,
235 VCAN, CTSS and FCN1. Non-classical monocytes appear to be the terminal cluster within the myeloid
236 differentiation trajectory and can be distinguished from non-classical monocytes by high expression of
237 surface CD16 and CD127, as well as FCGR3A, LST1 and MS4A1 on the transcriptomic level (Figure
238 N5i).

239 Next to the manifold myeloid differentiation stages, plasmacytoid dendritic cell progenitors (pDC prog)
240 and mature plasmacytoid dendritic cells (pDC), as well as both conventional dendritic cells of type 1
241 (cDC1) and type 2 (cDC2) are mapped (Figure N5j). On their surface, pDC progenitors express CD34
242 and CD133 and in addition high levels of CD38 and CD123. Moreover, they can be further characterized
243 by dim expression of CD33, CD45RA and Tim3, as well as high CD98 expression. Signature genes
244 highly expressed in pDC progenitors encompass IRF8, IL3RA, SHD and DNNT. Mature pDCs
245 gradually lose surface CD34 expression, remain positive for CD38 and also express higher levels of
246 CD45RA than their progenitors. Besides high CD123 expression, these cells can also be further
247 characterized by high surface expression of CD61, CD98 and CD4 as well as dim CD10 expression. On
248 the transcriptomic level, IRF8, IL3RA, CCDC50, CD4, TCF4 and DERL3 are highly expressed in
249 pDCs. Conventional dendritic cells of type 1 show dim levels of CD34 and CD133 surface expression,
250 and can be defined by high expression levels of CD33, CD11c, CD141 and Tim3. S100A10, FCER1A,
251 HAVCR2 and CD2 showed high mRNA expression levels in cDC1 cells. The second type of
252 conventional dendritic cells, cDC2, can be delineated by their absence of surface CD34 and CD133
253 expression, lower CD38, CD45RA and CD141 levels than their cDC1 counterparts and high expression
254 of CD11c, Tim3 and additionally CD1c. Transcriptionally cDC2 are similar to cDC1, however can be
255 further separated by higher expression of FCER1A, CD1C and HLA-DQB1.

256 Emanating from the Lympho-myeloid progenitor cluster, B cell commitment takes place, which is
257 accompanied by gradual elevation of CD10 surface expression. Cells within the first B cell
258 developmental stage, i.e. pre-pro B cells, express CD34 and dim levels of CD133 and CD38. CD10

259 expression is present, but to a significantly lower degree compared to later B cell differentiation stages.
260 Moreover, surface markers that are gradually upregulated in later stages, like CD19, CD81, CD24 or
261 CD9 are absent in this early differentiation stage. Pre-pro B cells and overall B cell commitment can be
262 further characterized by high expression of MME, VPREB1, CD79A and DNNT (Figure N5c).
263 Moreover, the transcription factor PAX5 is highly expressed at this differentiation stage (see WTA
264 expression data in Abseq-App). After the pre-pro B cell stage, cells enter and pass sequential stages, i.e.
265 the pro-B cell, and pre-B cell stages. Of note, our clustering splits pro-B cells and pre-B cells according
266 to distinct cell cycle states, which cells undergo being in early and late pro-B cell or pre-B cell stages.
267 Therefore, we labelled these clusters cycling pre-B and pro-B cells and non-cycling pre-B and pro B
268 cells (Figure N5c). In more detail, cells forming the former cluster are in a highly proliferative state
269 (high S-phase score, low G2/M score), whereas the latter are in a halted pre-mitotic, quiescent state, in
270 which DNA-rearrangements known as heavy and light chain rearrangements take place. In pro-B cells,
271 the latter state corresponds to cells that already underwent successful DJ-recombination at the Igm locus,
272 after which the above-mentioned proliferative state is entered, finally leading to VDJ rearrangement that
273 is accompanied by Rag2 expression (see WTA dataset in the Abseq-app). Successful heavy chain
274 rearrangement also marks the transition into the pre-B cell stage and to the expression of the so-called
275 pre-BCR, which corresponds to surface IgM coupled to surrogate light chains. IGHM mRNA expression
276 is increased upon entry into pre-B cell stage, accompanied by high proliferation, which terminates as
277 the cells enter the small pre-B cell stage in which Igk light chain rearrangement takes place. Successful
278 completion of all BCR rearrangements and surface expression of a functional BCR renders B cell entry
279 into the immature B cell stage.

280 Immature B cells are thought to exit the BM and start to transit through secondary lymphoid organs,
281 where final maturation events like isotype switching and somatic hypermutation occur. However, these
282 processes also occur in the bone marrow in germinal center-like structures (Cariappa, Chase, Liu,
283 Russell, & Pillai, 2007). B cells in that stage can be defined via CD9 surface expression, which is highest
284 in immature B cells, as well as expression of CD81, and in late stages CD272, CD20, and IgD, which
285 marks the start of isotype switching (Figure N5d). Importantly, immature B cells lack CD185
286 expression, which plays an important role for germinal center organization and is a signature surface
287 marker for subsequent maturation stages. CD9, CD79B, CD24 and TCL1A are highly expressed on the
288 transcriptional level at this stage. As expected, in late stages of the immature B cell cluster, isotype
289 switching from IgM to IgD can be observed, marking the transition to mature naïve B cells. Mature
290 naïve B cells express higher levels of surface CD5 than other B cell developmental stages, and
291 temporarily lower their CD24 surface expression. Cells at this stage also highly express IL4R and IGHD
292 mRNAs. Non-IgG-class switched B cells succeed mature naïve B cells and this stage can be
293 characterized by elevated surface expression of CD24, CD25, CD27, CD1c and IgD in the absence of
294 IgG expression (Figure N5d). High expression levels of CD82, CD27, JCHAIN and CD1C mRNAs are
295 transcriptomically characteristic for this stage. After B cells switched their isotype from IgD to IgG,
296 high surface IgG expression and absence of IgD expression can be observed (Figure N5d). Moreover,
297 transcriptionally class switched cells express elevated CD82, ITGB1 and ITGAM mRNAs. Adjacent to
298 class-switched B cells, a small cluster of CD11c+ memory B cells is apparent, whose exact biological
299 function remains elusive (Figure N5d). They have been described as putative progenitors of antibody
300 secreting plasma cells and have also been studied in the context of autoimmune diseases (Golinski et
301 al., 2020; Karnell et al., 2017). This cell subset is characterized by their high surface levels of CD11c,
302 IgG, dim levels of CD279 and lack of CD185 (CXCR5). Lack of CD185 expression indicates that cells
303 of this cluster are not present in follicular structures any longer. The final stage of B cell development
304 is represented by plasma cells, which express high surface levels of CD38, CD27 and CD54. On the
305 transcriptomic level, high expression of MZB1, DERL3, FKBP11 and SEC11C is observed in this
306 cluster.

307 Besides B cells, CD3+ positive T cells, which passed several differentiation stages in the thymus, re-
308 locate to the bone marrow. One can generally distinguish between alpha-beta T cells and gamma-delta
309 T cells, which describes an intrinsic difference in the respective T cell receptor (TCR) composition.
310 Alpha-beta T cells can be further separated in CD4+ and CD8+ T cells, that are either CD45+, CD3+,
311 TCRab+, CD4+ or CD45+, CD3+, TCRab+, CD8+ respectively. Of general note, inclusion of the
312 surface marker information greatly aids T cell annotation, as their RNA content is low and many gene
313 signatures are shared either between individual CD4+ and CD8+ T cell clusters or shared with other
314 cytotoxic cells, like natural killer cells.

315 Within the former, naïve CD4+ T cells can be further characterized by high expression of CD45RA,
316 CD28 and CD197 (CCR7) (Figure N5e). They are devoid of surface CD95, CD279 and CD25 and
317 further express high levels of CD4 mRNA, as well as CCR7, SELL and AIF1. Upon antigen encounter,
318 naïve T cells give rise to memory CD4+ T cells, which is accompanied by changes in their surface
319 proteome and transcriptome. Memory CD4+ T cells express CD28, don't express surface CD45RA or
320 CD197, and upregulate CD25 expression (Figure N5e). Transcriptionally, KLRB1, CCR6 and CD82
321 expression levels are elevated in this cell cluster. Besides memory CD4+ T cells, two more CD4 positive
322 clusters adopted a memory phenotype, but differed quite significantly to the former. We found one
323 cluster, which we termed cytotoxic CD4+ T cells, to be highly positive for cytotoxicity-related mRNAs
324 like GNLY, GZMA, NK7, and ADGRG1 and devoid of any CD28 expression (Figure N5e). The second
325 cluster, CD69+ CD4+ T cells, highly expressed CD69 and CD279 on its surface, and CD81, CST7,
326 TGFBI and HLA-DPBI mRNAs were elevated (Figure N5e). These cells likely constitute CD4 tissue
327 resident T cells, since both CD69 and CD279 are considered tissue resident memory T cell markers
328 (Kumar et al., 2017).

329 Naïve CD8+ T cells are transcriptionally highly similar to naïve CD4+ T cells, express high levels of
330 surface CD197 and, in contrast to their CD4+ T cell counterparts, express CD314. Furthermore, naïve
331 CD8+ T cells are lacking CD94, CD279 and CD103 surface protein expression (Figure N5f).
332 Transcriptionally, cells within this cluster highly express CCR7, SELL, and AIF1 mRNAs. Upon
333 antigen encounter, naïve CD8+ T cells adopt a central memory T cell phenotype, and are henceforth
334 termed CD8+ central memory T cells, which downregulate CD45RA surface protein and lack CD197,
335 CD103 and CD94 expression. Moreover, surface CD279 and CD81 is elevated in this cluster compared
336 to other bone marrow CD8+ T cell subsets (Figure N5f). Targeted mRNA readouts indicated high
337 expression of CD8A, DUSP1, CD74 and CCR5. A second memory phenotype cluster, termed CD8+
338 effector memory T cells, could be observed within CD8+ T cells, which showed substantial expression
339 of surface CD45RA, CD226, and CD94 in the absence of CD103, CD279, CD27, CD28 expression
340 (Figure N5f). Cells within this cluster express high levels of genes involved in cytotoxicity related
341 processes. Another prominent cluster showing a memory T cell phenotype were CD8+ CD103+ tissue
342 resident memory T cells. They can be characterized by high surface expression of CD103, CD25 and
343 CD26 in the absence of CD45RA and CD197 expression (Figure N5f). On the transcriptional level,
344 these cells robustly express IL7R, ITM2C and DPP4 mRNAs.

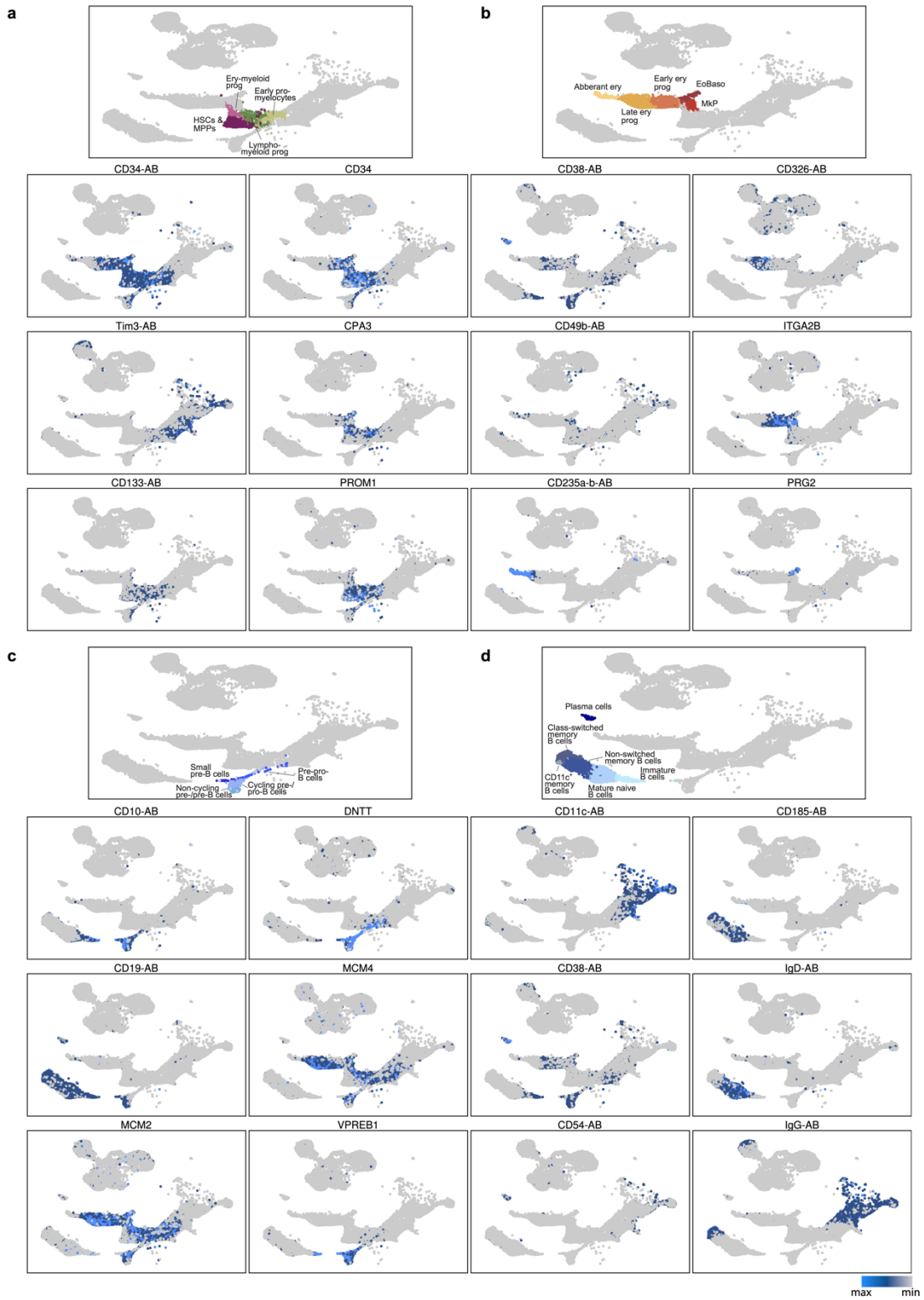
345 Besides CD4+ and CD8+ $\alpha\beta$ -T cells, $\gamma\delta$ -T cells, are apparent in our dataset. Within that $\gamma\delta$ -T cells
346 cluster, one subset was highly positive for surface CD226, CD26, CD94 and negative for CD45RA
347 expression (Figure N5g). In the second subset, CD26, CD226 and CD94 expression is absent or only
348 dim, but TCR- $\gamma\delta$ (clone B1) is highly expressed (Figure N5g). Interestingly, TCR- $\gamma\delta$ antibody clone B1,
349 which is present in the 97 Ab panel seems to be less efficient in $\gamma\delta$ -T cell detection than clone 11F2,
350 which was present in the 197 Ab panel (Extended Data Fig. 4). The anti-Vd2 TCR antibody (clone B6)
351 uniquely labels the CD226+ CD26+ CD94+ CD45RA- subset and leaves the other subset unstained. We
352 therefore recommend using both anti-Vd2 (B6) and anti TCR- $\gamma\delta$ (11F2) for improved $\gamma\delta$ -T cell
353 detection. On the transcriptional level, KLRB1, TRDC, TRGC and DPP4 were highly expressed in this
354 cluster.

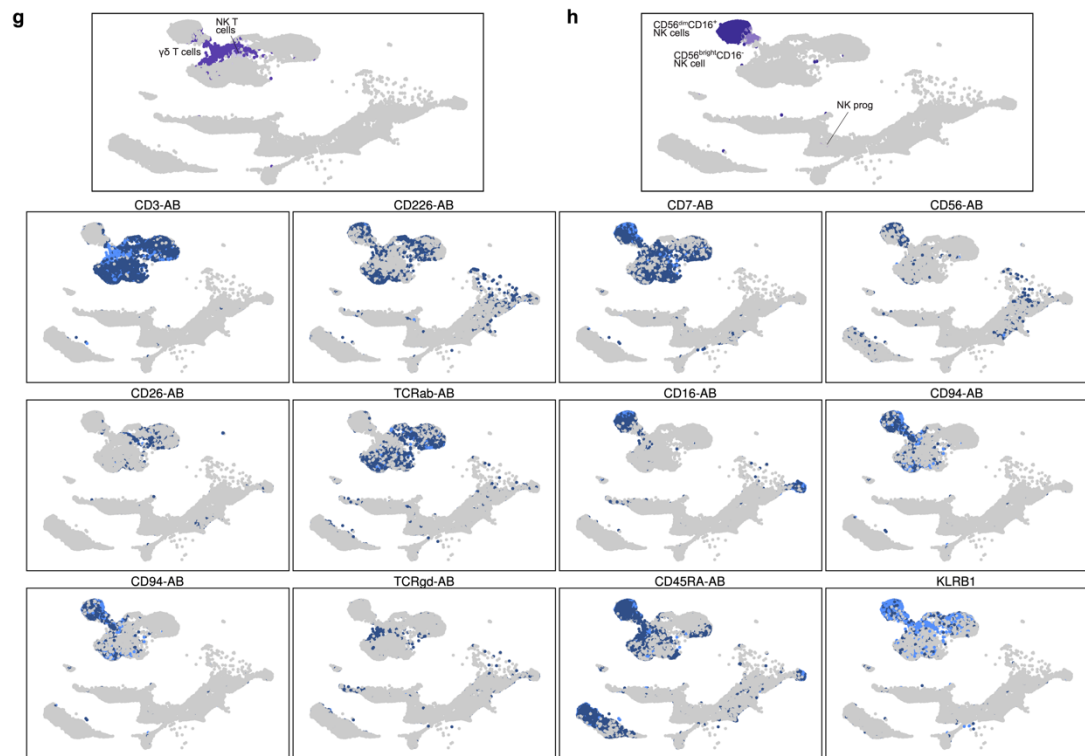
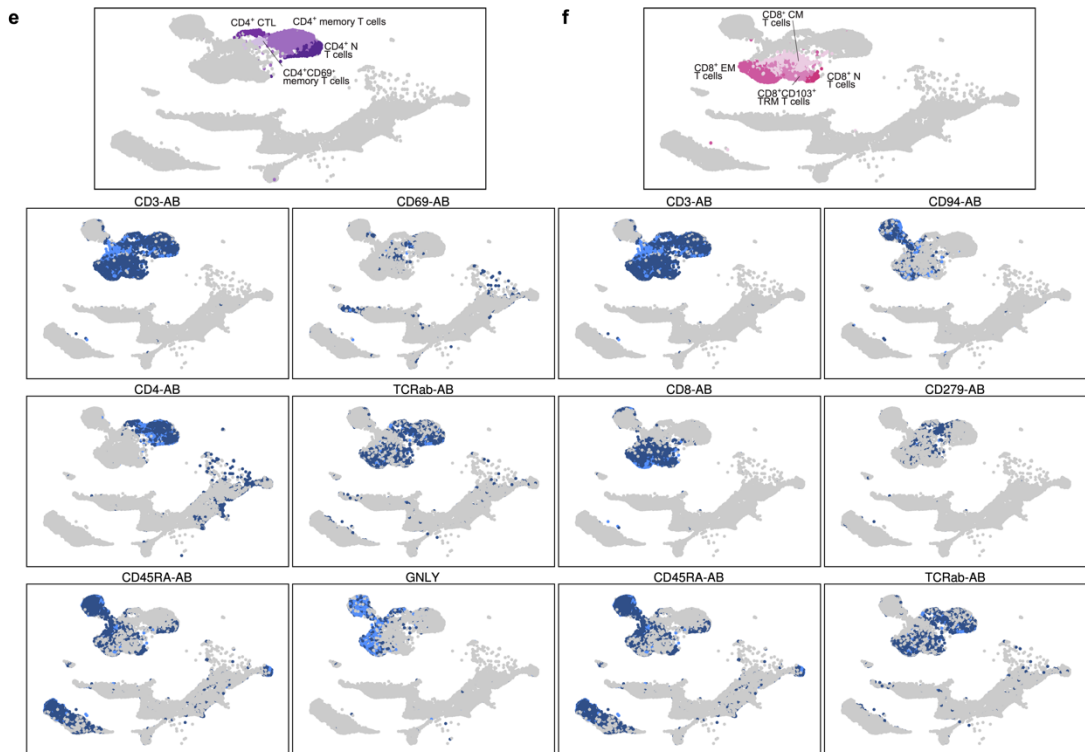
355 The second CD3+ TCR $\alpha\beta$ -negative cluster are putative natural killer T cells (NKT cells), that can be
356 characterized by elevated CD69 and CD314 surface expression, which were accompanied by dim
357 binding of the TCR $\gamma\delta$ antibody (clone B1).

358 Next to CD3+ T cells, two well-known natural killer (NK) cell clusters, namely CD56^{dim} CD16+ and
359 CD56^{bright} CD16- NK cells, are present in our dataset. Both subsets are readily identified via high surface
360 expression of CD45, CD7, CD94 and CD45RA (Figure N5h). CD56^{bright} CD16- NK cells express higher
361 levels of CD56 and CD335, as well as lower levels of CD16 on their surface. In contrast, CD56^{dim}
362 CD16+ NK cells have higher surface levels of CD16, CD127 and CD152. The latter are thought to be
363 more cytotoxic, which is also reflected in the transcriptional differences between the two subsets.
364 Compared to other clusters in the dataset, generally cytotoxic mRNAs are highly expressed in these two
365 clusters. In addition, a small cluster located in proximity of HSCs and MPPs was particularly interesting,
366 as it expressed mature NK surface markers like CD16, CD56 and CD7 as well as surface markers
367 specific for immature progenitor cells like CD34 and CD133 ((Figure N5a and N5h). A similar
368 phenotype was observed at the mRNA level, as these cells both expressed mature NK mRNAs like
369 NKG7 or KLRK1 and stem and progenitor specific mRNA like CRHBP, CD34 and NPR3. We therefore
370 named this cluster NK cell progenitor. Besides healthy hematopoietic cells, at least one mesenchymal
371 stromal cell (MSC) cluster is present in our dataset (Figure N5k). MSC cluster 1 was characterized by
372 high surface expression of CD10, CD13, CD26 and CD49a, which was accompanied by typical MSC
373 gene expression like CXCL12 and SPARC. Putative MSC cluster 2 expressed antibodies found in
374 scavenger cells like macrophages, such as CD206, CD141, CD163 and CD16, but also expressed
375 CXCL12 suggesting a mixed composition and some degree of heterogeneity.

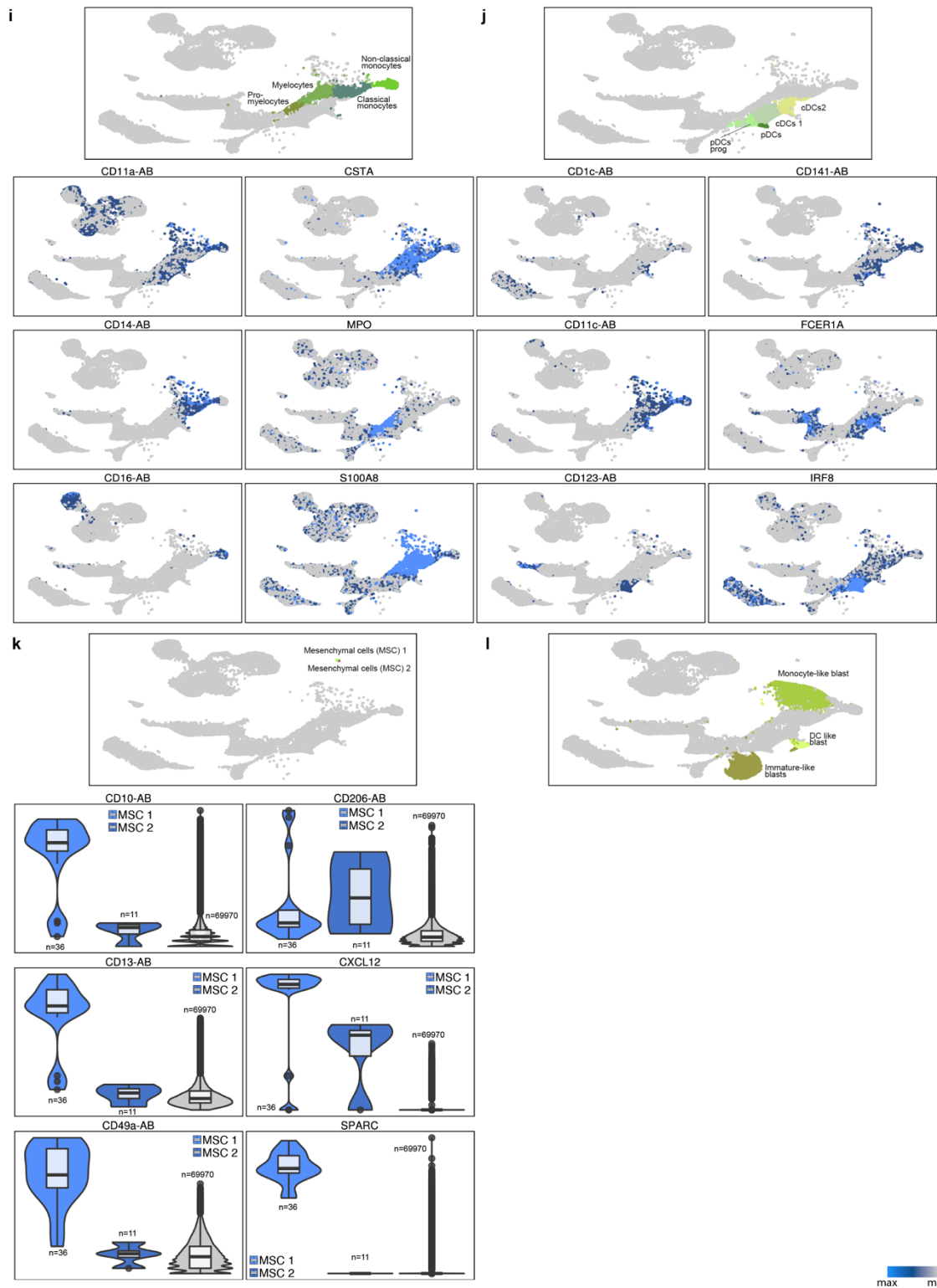
376 All clusters described above were consistently identified in six healthy BM donors. In the reference
377 AML patients (n=3, Figure 1b), we were able to determine three additional cell clusters. Some of these
378 were either specific for individual AML samples or a mix of cells from different AML patients.
379 Regarding the latter, the cluster annotated as immature blasts is a mixture of cells from all three patients.
380 Cells within this cluster have heterogeneous surface phenotypes and share similarities with different
381 healthy cell types (Figure N5l).

382





max min



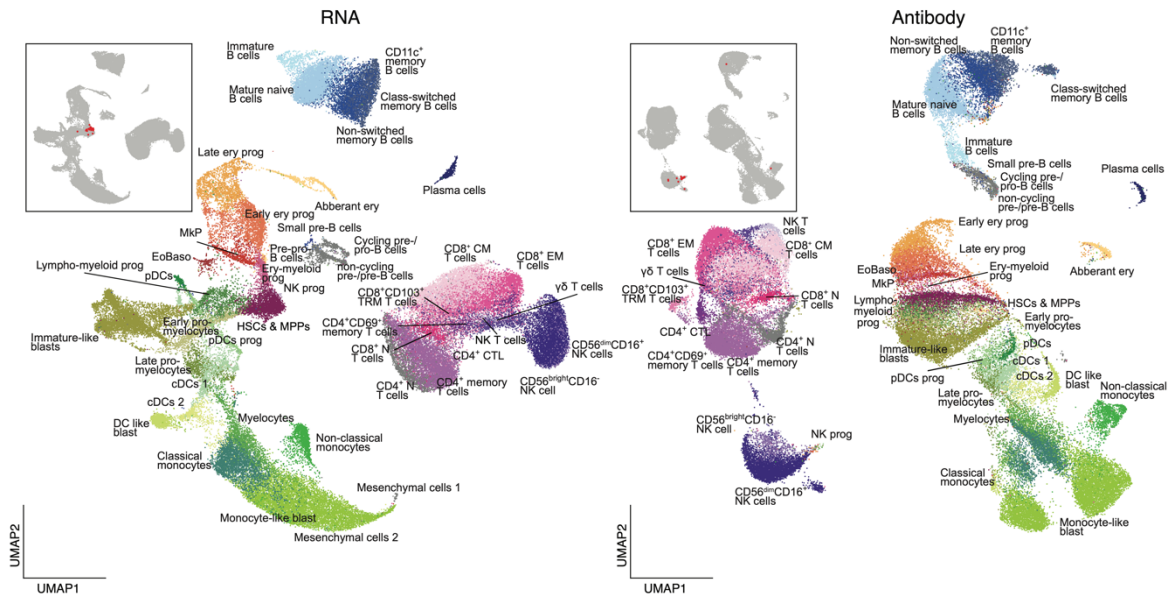
386
387
388
389
390
391
392

Figure N5. Cell type annotation. Both mRNA and surface protein expression were considered for annotation, and several exemplary plots for either mRNA or surface protein expression are shown. Cell types depicted in the UMAPs visualizations were grouped into biological subgroups. Sample size: MSC1 n=36, MSC2 n=11, others n=69970. See methods, section *Data visualization* for a definition of boxplot elements.

393 **Supplementary Note 6: Inclusion of surface marker data improves cell type classification**

394 In order to determine the utility of RNA and surface marker expression for resolving cell types and cell
395 stages, we performed UMAP visualizations using either RNA or surface marker information (Figure
396 N6) or UMAP visualization after MOFA-UMAP multi-omic integration of RNA and surface markers
397 (Figure 1b). Interestingly, dependent on the cell type, RNA or surface marker information were more
398 powerful in separating cell types and cell stages (Figure N6). For example, for the HSPC compartment,
399 RNA was superior over surface markers in resolving cell states, while B cell stages and the myeloid
400 compartment were more efficiently separated using surface markers (Figure N6). Most importantly, the
401 combined information of both layers provided the highest resolution not achieved by any of the
402 individual layers alone (compare to Figure 1b). Interestingly, NK cell progenitors, a subset that we
403 found to contain both features of mature NK cells (surface: CD56, CD7, mRNA: NKG7, KLRK1) and
404 hematopoietic stem and progenitor cells (surface: CD34, CD133, mRNA: CD34, CRHBP, NPR3) was
405 grouped with the HSPC compartment when only using RNA markers and with the NK cell compartment
406 when only using the surface markers. Only in the joined view (Figure 1b), these cells formed an
407 independent cluster, identifying a cell population that has hitherto remained hidden. Similarly, T cell
408 subpopulations were resolved much better when using information from both omics layers. For example,
409 populations such as $\gamma\delta$ -T cells and NK T cells did not form an independent group in either of the
410 individual layers and information from both layers was required to resolve them. In addition, usage of
411 surface markers improves the separation between cytotoxic T cells and NK cells.

412
413 Our results imply that during stem cell differentiation, mRNA expression is a relatively early step in the
414 process of commitment, compared to surface protein expression. In line with that, we and others have
415 consistently observed lineage priming signatures in cells that surface phenotypically appear immature
416 (see Figure 6d, Extended Data Fig. 9a, b and see also Paul et al., 2015; Velten et al., 2017). By contrast,
417 in mature cell stages, cellular identity is firmly established and reflected both in the transcriptome, and
418 on surface protein expression. In these mature cell types, antigen expression adds information to mRNA
419 expression alone for three reasons: First, especially in T cells, mRNA measurements are often noisy due
420 to the low RNA content of the cells. Second, in T cells and B cells, the annotation of cell types has
421 historically been performed using surface antigens. Relatively similar cell states may have therefore
422 been classified as functionally different based on the expression of a single marker, as in the case of
423 class-switched vs. non-switched memory B cells, that mostly differ in the expression of surface
424 immunoglobulins (IgM, IgD vs. IgG, IgA) while maintaining a very similar transcriptome. Third, a
425 technical reason for our observations may be that the antibody panel (97 antibodies selected based on
426 availability) can be biased towards providing higher resolution in specific cell types, whereas the mRNA
427 panel was designed more systematically (see Supplementary Note 1).



428
 429 **Figure N6. Inclusion of surface marker data improves cell type classification.** UMAP visualization
 430 was calculated using either only RNA, or only surface marker expression. NK progenitor cells are
 431 highlighted in red. A UMAP visualization containing the combined information of RNA and surface
 432 markers is displayed in the main *Figure 1b*.

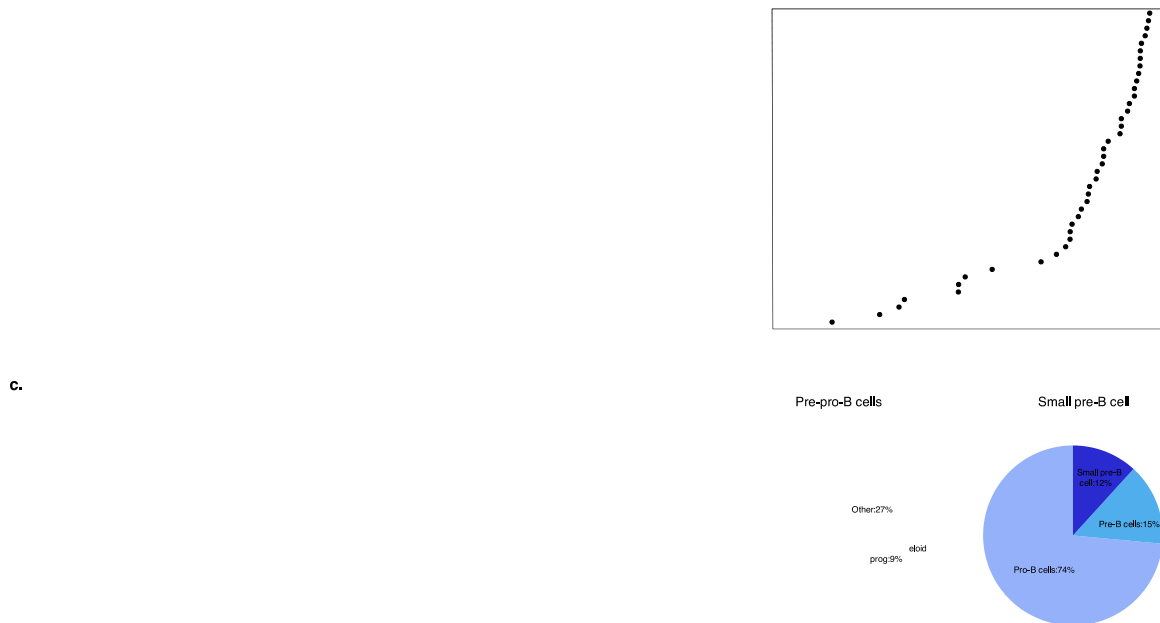
433 **Supplementary Note 7: Validation of query datasets projections**

434 To project new “query” single cell RNA-seq data on the reference atlas, the reference was subset to
 435 include only cells from the healthy individuals. For every query cell, we then determined the five nearest
 436 neighbors using scmap (Kiselev, Yiu, & Hemberg, 2018). The median UMAP position and cell type
 437 label of the five neighbors was then computed. For projecting on pseudotime, the average pseudotime
 438 value of the neighbors was computed if they were part of a given trajectory, i.e. not classified NA. The
 439 high accuracy of this mapping strategy was confirmed using both the 200-antibody experiment and the
 440 whole transcriptome experiment (Supplementary Note 2); in both cases, projected cell types had the
 441 same marker gene expression pattern as the cell types used in the original annotation.

442
 443 For a more quantitative analysis, we evaluated the effectivity of this approach by projecting the healthy
 444 reference against itself. For a randomly selected set of cells, we showed that cells consistently projected
 445 very close to their original location (Figure N7a); the only exception were cells falling into the very
 446 heterogeneous and small class of MSC2. We then calculated the precision of the projection as the
 447 proportion of correctly assigned cell type labels (Figure N7b). This showed that for most cell types the
 448 projection and mapping of the cell type had a precision higher than 0.8, with just a few populations
 449 having a lower precision, likely due to projection to a very similar cell state (Figure N7c).

450
 451 The entire workflow of projection on the reference, differential expression testing and estimation of
 452 inter-patient variability is available at <https://git.embl.de/triana/nrn>

453



454
 455 **Figure N7. Evaluation of self-projection on the healthy reference.** a. Precision of the cell type
 456 assignment base on the projection of the healthy reference against itself using scMAP. b. UMAP
 457 projection of one cell of each cell type (red) against the whole reference (gray) and the connection
 458 between the original coordinate and the projected one (blue). c. Distribution of the cell type projection
 459 in representative cell types with low assignment precision.
 460

461 **Supplementary Note 8: Smart-seq2 validation**

462 To validate markers identified in Figure 2 and 3, and gating panels described in Figure 6, we performed
 463 two experiments that couple FACS-based indexing of surface markers to single-cell RNAseq (“index
 464 scRNAseq”). For this purpose, we used Smart-seq2 and successfully sequenced 630 single cells that
 465 were stained with the data-defined classification panel established in Figure 6, and 330 single cells that
 466 were stained with a semi-automated panel aiming at resolving the erythro-myeloid differentiation of
 467 HSCs. The semi-automated panel included the backbone from the classification panel, but additionally
 468 contained the well-known erythroid priming marker CD71 (encoded by TFRC), the newly identified
 469 erythroid commitment marker CD326 (Figure 3), the eosinophil-basophil progenitor marker FcER1A,
 470 as well as CD49b, a marker highly expressed in megakaryocyte progenitors. Additionally, we included
 471 1035 cells from a previously published HSPCs dataset (Velten et al., 2017) with indexed single-cell
 472 RNAseq using the classical Doulatov gating scheme (Doulatov et al., 2010) into the analysis. To
 473 visualize our data, we performed dimensional reduction by Principal Components Analysis (PCA) and
 474 UMAP. We identified groups of similar cells using Shared Nearest Neighbor (SNN) clustering followed
 475 by data integration using canonical correlation analysis and mutual nearest neighbors as implemented
 476 in Seurat v3. A UMAP representation of the integrated dataset demonstrated a successful data
 477 integration (Figure N8a). Unsupervised clustering revealed the presence of multiple cell subpopulations
 478 adequately representing HSPC differentiation (Figure N8b). For all clusters we identified markers
 479 defined as those with the highest classification power as measured by the area under the receiver
 480 operating characteristics curve (AUC). The top five markers per cell type are shown in Figure N8d. Cell
 481 type labels (Figure N8c) were determined using the same marker genes as for the main Abseq data set
 482 (see Supplementary Table 4 and Supplementary Note 5).
 483

509 **References**

- 510 Cariappa, A., Chase, C., Liu, H., Russell, P., & Pillai, S. (2007). Naive recirculating B cells mature
511 simultaneously in the spleen and bone marrow. *Blood*, *109*(6), 2339–2345.
512 <https://doi.org/10.1182/blood-2006-05-021089>
- 513 Doulatov, S., Notta, F., Eppert, K., Nguyen, L. T., Ohashi, P. S., & Dick, J. E. (2010). Revised map of
514 the human progenitor hierarchy shows the origin of macrophages and dendritic cells in early
515 lymphoid development. *Nature Immunology*, *11*(7), 585–593. <https://doi.org/10.1038/ni.1889>
- 516 Golinski, M. L., Demeules, M., Derambure, C., Riou, G., Maho-Vaillant, M., Boyer, O., ... Calbo, S.
517 (2020). CD11c+ B Cells Are Mainly Memory Cells, Precursors of Antibody Secreting Cells in
518 Healthy Donors. *Frontiers in Immunology*, *11*. <https://doi.org/10.3389/fimmu.2020.00032>
- 519 Karnell, J. L., Kumar, V., Wang, J., Wang, S., Voynova, E., & Ettinger, R. (2017, November 1). Role
520 of CD11c+ T-bet+ B cells in human health and disease. *Cellular Immunology*, Vol. 321, pp. 40–
521 45. <https://doi.org/10.1016/j.cellimm.2017.05.008>
- 522 Kerkelä, E., Lahtela, J., Larjo, A., Impola, U., Mäenpää, L., & Mattila, P. (2019). *Exploring*
523 *transcriptomic landscapes in red blood cells, in their extracellular vesicles and on a single-cell*
524 *level*. <https://doi.org/10.21203/rs.2.14503/v1>
- 525 Kiselev, V. Y., Yiu, A., & Hemberg, M. (2018). Scmap: Projection of single-cell RNA-seq data across
526 data sets. *Nature Methods*, *15*(5), 359–362. <https://doi.org/10.1038/nmeth.4644>
- 527 Kowalczyk, M. S., Tirosh, I., Heckl, D., Rao, T. N., Dixit, A., Haas, B. J., ... Regev, A. (2015).
528 Single-cell RNA-seq reveals changes in cell cycle and differentiation programs upon aging of
529 hematopoietic stem cells. *Genome Research*, *25*(12), 1860–1872.
530 <https://doi.org/10.1101/gr.192237.115>
- 531 Kumar, B. V., Ma, W., Miron, M., Granot, T., Guyer, R. S., Carpenter, D. J., ... Farber, D. L. (2017).
532 Human Tissue-Resident Memory T Cells Are Defined by Core Transcriptional and Functional
533 Signatures in Lymphoid and Mucosal Sites. *Cell Reports*, *20*(12), 2921–2934.
534 <https://doi.org/10.1016/j.celrep.2017.08.078>
- 535 Paul, F., Arkin, Y., Giladi, A., Jaitin, D. A., Kenigsberg, E., Keren-Shaul, H., ... Amit, I. (2015).
536 Transcriptional Heterogeneity and Lineage Commitment in Myeloid Progenitors. *Cell*, *163*(7),
537 1663–1677. <https://doi.org/10.1016/j.cell.2015.11.013>
- 538 Schraivogel, D., Gschwind, A. R., Milbank, J. H., Leonce, D. R., Jakob, P., Mathur, L., ... Steinmetz,
539 L. M. (2020). Targeted Perturb-seq enables genome-scale genetic screens in single cells. *Nature*
540 *Methods*, *17*(6), 629–635. <https://doi.org/10.1038/s41592-020-0837-5>
- 541 Stuart, T., Butler, A., Hoffman, P., Hafemeister, C., Papalexi, E., Mauck, W. M., ... Satija, R. (2019).
542 Comprehensive Integration of Single-Cell Data. *Cell*, *177*(7), 1888–1902.e21.
543 <https://doi.org/10.1016/j.cell.2019.05.031>
- 544 Velten, L., Haas, S. F., Raffel, S., Blaszkiewicz, S., Islam, S., Hennig, B. P., ... Steinmetz, L. M.
545 (2017). Human haematopoietic stem cell lineage commitment is a continuous process. *Nature*
546 *Cell Biology*, *19*(4), 271–281. <https://doi.org/10.1038/ncb3493>
- 547 Velten, L., Story, B. A., Hernandez-Malmierca, P., Milbank, J., Paulsen, M., Lutz, C., ... Steinmetz,
548 L. M. (2018, December 21). MutaSeq reveals the transcriptomic consequences of clonal
549 evolution in acute myeloid leukemia. *BioRxiv*, p. 500108. <https://doi.org/10.1101/500108>
- 550 Young, M. D., & Behjati, S. (2020). SoupX removes ambient RNA contamination from droplet-based
551 single-cell RNA sequencing data. *GigaScience*, *9*(12).
552 <https://doi.org/10.1093/gigascience/giaa151>

553

554